

X-ray optics in new instruments for astro- and astroparticlephysics

PhD thesis of
Anders Clemen Jakobsen

Kongens Lyngby 2014
Compiled: July 14, 2014

DTU Space
National Space Institute

Technical University of Denmark
Building 327, DK-2800 Kongens Lyngby, Denmark
Phone +45 45253351, Fax +45 45882673
www.space.dtu.dk

Compiled: July 14, 2014 at 18:12
ISSN 0909-3192

Summary

This is the summary/abstract

Resumé

På dansk ...

Preface

!!!!!!PLACEHOLDER!!!!!!

This thesis was prepared at Informatics Mathematical Modelling, the Technical University of Denmark in partial fulfillment of the requirements for acquiring the Ph.D. degree in engineering.

The thesis deals with different aspects of mathematical modeling of systems using data and partial knowledge about the structure of the systems. The main focus is on extensions of non-parametric methods, but also stochastic differential equations and neural networks are considered.

The thesis consists of a summary report and a collection of ten research papers written during the period 1996–1999, and elsewhere published.

Lyngby, August 2014

Anders Clemen Jakobsen

Papers included in the thesis

- [A] Anders C. Jakobsen, Desiree Della Monica Ferreira, Finn E. Christensen, Brian Shortt, Max Collon, Marcelo D. Ackermann; Preliminary coating design and coating developments for ATHENA. *Proc. SPIE 8147, Optics for EUV, X-Ray, and Gamma-Ray Astronomy V*, 81470T (October 06, 2011);
- [B] Anders C. Jakobsen, Michael J. Pivovarov, Finn E. Christensen; X-ray optics for axion helioscopes. *Proc. SPIE 8861, Optics for EUV, X-Ray, and Gamma-Ray Astronomy VI*, 886113 (September 26, 2013)

Acknowledgements

I thank my...

Contents

Summary	i
Resumé	iii
Preface	v
Papers included in the thesis	vii
Acknowledgements	ix
1 Introduction	1
1.1 X-ray optics described	1
1.2 X-ray telescopes described	1
2 Designing a telescope	3
2.1 This is a new section	3
3 DTU Space coating facility	5
3.1 Overview	5
3.2 Laboratory setup	6
3.3 Multilayer coating chamber	7
3.4 Multilab control software	8
4 Coatings for ATHENA	9
4.1 Investigating the baseline Ir/B ₄ C coating	9
4.2 Alternative coatings	9
4.3 Findings from long term storage	9
4.4 Novel coating methods	9

5 Coatings for CAST 11
5.1 This is a new section 11

A Preliminary coating design and coating developments for ATHENA 13

B X-ray optics for axion helioscopes 23

CHAPTER 1

Introduction

Introduction to chapter 1.

1.1 X-ray optics described

1.2 X-ray telescopes described

1.2.1 This is a new subsection

CHAPTER 2

Designing a telescope

2.1 This is a new section

2.1.1 This is a new subsection

CHAPTER 3

DTU Space coating facility

This chapter is written as a manual and introduction for future students and employees who wish to use the multilayer coating facility at DTU Space. Several of the sections, such as those describing the development of the control software are not necessary for anything but to give a background on the considerations taken in the process.

3.1 Overview

The multilayer coating facility is the vacuum chamber placed in the laboratory that is otherwise known as the Multilab. It started out as a vapor deposition chamber for the SODART mission. Capable of vaporising a gold wire with a W rod in the center of the chamber, it would deposit a layer of gold on any mirror facing the center. The chamber was later upgraded with magnetrons, each with independent shutters.

The magnetrons and attached powerful DC power supplies could deposit films atom-by-atom instead of larger gold particles that would come from vaporisation. The upgrade made it possible to coat multilayers with d-spacings thinner than 3 nm and eventually became the coating method used for the NuSTAR mission.

The entire lab was moved from Rockefeller Institute near Rigshospitalet in Copenhagen during the summer of 2012. It was up and running again around the summer of 2013 in the newly constructed building 328, the new home for DTU Space on DTU campus. In the new location, the lab is 50% larger, has a double airlock (earlier just a single airlock), laminar airflow from ceiling mounted HEPA filters and various other improvements. The result is a considerably cleaner facility, which is important to avoid contaminants on optical substrates.

3.2 Laboratory setup

The vacuum chamber is the dominant piece of the laboratory, and most of the computers, electronics and cooling in the lab is in some way connected to the chamber. Apart from the chamber, the lab consists of a downflow module, two fume hoods, a profilometer, a large clean room oven, and various tables and cupboards. Next to the lab is the Multilab Auxilliary Room, which houses the cooling heat exchangers and pumps, the rotary vane roughing pump, DC power supplies, and a large part of the extra storage needed for the lab. Additionally, there is a room in the basement that houses a ceramic oven that has a built in vacuum chamber and also serves to store hundreds of spare pieces of NuSTAR optic glass.

3.2.1 Downflow module

The downflow module is where the

3.2.2 Fume hoods

3.2.3 Oven

3.2.4 Multilab auxilliary room

3.2.5 Multilab basement storage

3.2.6 Profilometer

3.3 Multilayer coating chamber

3.3.1 Chamber, pumps & valves

Bell

Viton ring

Heaters

Roughing pump

Turbo pump

3.3.2 Cathodes

Powersupplies

Masks

3.3.3 Gas flow controllers

3.3.4 Pressure gauges

Baratron

3.3.5 Rotating ring

3.3.6 Cathode shutters

3.4 Multilab control software

3.4.1 The original software solution

3.4.2 Considerations on a new software solution

CHAPTER 4

Coatings for ATHENA

4.1 Investigating the baseline Ir/B₄C coating

4.2 Alternative coatings

4.3 Findings from long term storage

4.4 Novel coating methods

4.4.1 Pulsed-DC sputtering

4.4.2 Reactive sputtering with N₂

CHAPTER 5

Coatings for CAST

5.1 This is a new section

5.1.1 This is a new subsection

APPENDIX A

Preliminary coating design and coating developments for ATHENA

Publication printed in *Proc. SPIE, Optics for EUV, X-Ray, and Gamma-Ray Astronomy V.*

Preliminary coating design and coating developments for ATHENA

Anders C. Jakobsen^a, Desiree Della Monica Ferreira^a, Finn E. Christensen^a, Brian Shortt^b,
Max Collon^c, Marcelo D. Ackermann^c

^aDTU Space, Juliane Maries Vej 30, 2100 Copenhagen Ø, Denmark);

^bEuropean Space Research and Technology Ctr. (Amsterdam, Netherlands)

^cCosine Research B.V. (Leiden, Netherlands)

ABSTRACT

We present initial novel coating design for ATHENA. We make use of both simple bilayer coatings of Ir and B₄C and more complex constant period multilayer coatings to enhance the effective area and cover the energy range from 0.1 to 10 keV. We also present the coating technology used for these designs and present test results from coatings.

1. INTRODUCTION

In this paper we investigate the possibility of increasing the ATHENA telescope effective area in the range between 0.1 and 10 keV. We studied the performance of five different material combinations, W/Si, Ir/B₄C, Pt/C, Pt/B₄C and Mo/Si, considering a simple bilayer, simple multilayers and linear graded multilayers. To reduce stress in the Ir/B₄C coating, we investigated the need of a third stress reducing material as an undercoat to the Ir/B₄C bi-layer.

The ATHENA mission consists of two identical telescopes with fixed focal planes, the first containing a calorimeter spectrometer and the second a wide field imager. The ATHENA focal plane is of 11.5 m, the telescopes innermost radius of 0.15 m and outermost radius of 0.90 m. The operational energy range is from 0.1 to 10 keV.

The coating recipe adopted as baseline is a bilayer with an 8 nm layer of B₄C on top of a 10 nm Ir layer. The same coating is adopted for all mirror modules at all radii.

2. OPTIMIZING ATHENA COATING DESIGN - PRELIMINARY RESULTS

2.1 Low energy range

The choice for radii division and coating recipes is based on the need of optimization at different energy ranges. The use of a simple bilayer coating is appropriate for energies lower than 5 keV, while to improve the telescope performance above 5 keV the use of multilayers is required.

The telescope radius where simple bi-layers should be applied is considered to be the radius at which the reflectance of the Ir/B₄C baseline coating at 6 keV is above 30%. This is a somewhat arbitrary choice and considered as a good starting point for investigation. This radius corresponds to the seven innermost rows of mirror modules, see figure 1. The optimization of bi-layer coating is performed for this region (radius between 0.15 m to 0.59 m).

The criterion applied for the choice of a simple bilayer coating material is based on the coating performance at 1 keV and 6 keV considering the seven innermost rows of mirror modules.

We computed the best coating thickness for each material combination in order to maximize the effective area at 1 keV and 6 keV. The surface roughness considered is 0.65 nm for Ir/B₄C, and 0.45 nm for W/Si, Pt/C,

Further author information: (Send correspondence to A.C.J.)

A.C.J.: E-mail: jakobsen@space.dtu.dk, Telephone: +45 3532 5735

D.D.M.F.: E-mail: desiree@space.dtu.dk, Telephone: +45 3532 5734

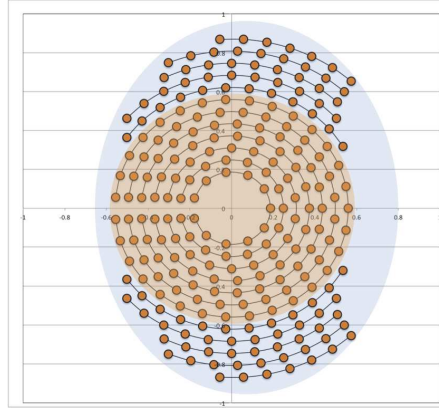


Figure 1. Diagram of one of two telescope optics for ATHENA. Each orange circle represents a mirror module with 68 coated SPO substrates. The inner part chosen for simple bilayer/trilayer and outer part chosen to carry a multilayer with cap layer and top layer.

Pt/B₄C and Mo/Si. We observe that Pt/B₄C presents superior effective areas at both energies, followed by Ir/B₄C.

Because the material combination of Pt/B₄C is still unknown at the present time, and properties such as roughness and stress need further investigation, Ir/B₄C is considered as the best option for a bi-layer coating.

We investigate the best layer thickness to maximize the on-axis effective area at 6 keV considering a Ir/B₄C coating. As the effective area scales with the reflectivity square, we base our study on the reflectivity curve computed at this energy. To optimize the Ir/B₄C coating we vary the thicknesses of Ir and B₄C and compute the on-axis effective area at 1 keV and at 6 keV. We list the parameter combinations that provide maximum effective area at those energies and parameter combinations resulting in 99% and 95% of the maximum effective area. The best parameter combination provides minimal loss of on-axis effective area on both energies. Based on the on-axis effective areas at 1 keV and 6 keV and on the layer thickness we find that the baseline (10 nm Ir, 8 nm B₄C) is the optimum choice.

2.2 Mid energy range

At radii beyond the seven innermost mirror module rows (0.59 m) the bi-layer reflectivity is inefficient at energies above 6 keV. To enhance the telescope effective area at the energy range from 5 to 10 keV, we suggest a multilayer coating approach for the 5 outermost mirror module rows.

Also here the material choice is defined by evaluating the on-axis effective area at 6 keV for this region (0.59–0.90 m). We consider a simple multilayer coating for the same materials listed above, a cap layer of the heaviest material and an 8 nm overcoat of B₄C to account for the energies below 1.5 keV. The surface roughness applied is 0.65 nm for Ir/B₄C and 0.45 nm for the remaining material combinations.

The parameters considered in the computation are: number of bi-layers, thickness of the bi-layers, ratio between heavy and light material thickness and thickness of the extra layer of the heavy material. The best parameters for each material choice return maximum on-axis effective area at 6 keV.

Applying a multilayer of W/Si results in the best performance considering the criterion above with the second best options being Pt/B₄C and Pt/C with equivalent performances. The material combinations Pt/B₄C and Pt/C return on-axis effective areas that differ from the computed for W/Si by only 2%. There are several reasons for choosing Pt over W, e.g. the absorption edges around 1–2 keV, and those aspects are under investigation. At this point we proceed with the optimization of the telescope outermost rows considering W/Si as the best material choice for multilayer coating.

2.3 Multilayer optimization

The actual ATHENA coating baseline presents optimal performance at energies below 5 keV but the use of multilayers in the outer mirror module rows can increase the telescope effective area at energy range 5 to 10 keV. The optimum coating design so far is a bi-layer of Ir/B₄C with thickness of 10 nm and 8 nm respectively, applied to the seven innermost mirror module rows. The remaining five outermost rows are optimized considering multilayers of W/Si with a W cap layer and an 8 nm B₄C overcoat.

To optimize the coating design at the telescope outermost region we considered five different coating recipes, one for each row. The motivation for this choice is the need of a smooth effective area curve at the scientifically interesting region around 6 keV.

A linear graded multilayer is chosen over a simple multilayer in order to optimize a wider energy range. The design for optimization is therefore a linear graded W/Si multilayer with a W cap layer on top of the multilayer and an 8 nm B₄C overcoat. The B₄C overcoat is optimized for best performance at 1 keV and is therefore set to 8 nm.

For each row in the region between 0.59 m and 0.90 m an optimal coating recipe is computed in order to maximize the effective area in the region around 6 keV without compromising the effective area at lower energies. This is achieved by evaluating the several possible parameter combinations that result in the maximum integrated effective area over energy for the energy range between 3 keV and 8 keV with the condition that the loss of effective area between 1.5 and 5 keV is minimal. To achieve that we look at how the gradient of the on-axis effective area changes over the energy range between 3 keV and 8 keV and look for solutions returning maximum effective area with minimum gradient, i.e. the curve should be as flat as possible. This approach is preliminary and alternative choices for the figure of merit are being investigated.

The parameters considered in this computation are: Number of W/Si bi-layers (n), thickness ratio between W and Si (Si-Γ), minimum bi-layer thickness (d_{\min}), maximum bi layer thickness (d_{\max}) and thickness of the W cap layer (d_W) (to accommodate the energies between 1.5 keV and 5 keV). The parameters were varied considering steps of 10 bilayers, 0.1 for Si-Γ, 0.5 nm for d_{\min} and d_{\max} and 1 nm for d_W .

The best parameters for each row are listed in table 1. The optimized effective area over energy is shown in figure 2. The comparison between the baseline performance at 1 keV and 6 keV is shown in table 2.

Row	n	Si-Γ	d_{\min} [nm]	d_{\max} [nm]	d_W [nm]
8	10	0.5	5.5	7.5	8.0
9	10	0.5	5.0	7.5	8.0
10	20	0.6	4.0	7.0	7.0
11	30	0.7	3.5	6.5	6.0
12	20	0.6	4.0	6.5	6.0

Table 1. Optimized coating design for the outermost mirror module rows of ATHENA assuming a linear graded multilayer

	Baseline	Optimized
A_{eff} at 1 keV [m ²]	1.146	1.152 (+0.4 %)
A_{eff} at 6 keV [m ²]	0.431	0.454 (+5.6 %)

Table 2. Effective area of ATHENA. Results listed for 2 telescopes with a 10% reduction applied to account for eventual losses due to e.g. alignment and particle contaminations.

3. SILICON PORE OPTIC SUBSTRATES

The optics of ATHENA will consist of >60,000 Silicon Pore Optic (SPO) mirror substrates.¹ Each substrate is cut from a wafer in sizes of 66 mm x 66 mm and have grooves cut into the bottom side so the substrate gets thin ribs, which gives the substrates the ability to be stacked directly on top of each other. The top surface of the substrate is treated with a SiO₂ wedge with a specific slope so each SPO substrate has the right angle to the focal plane.

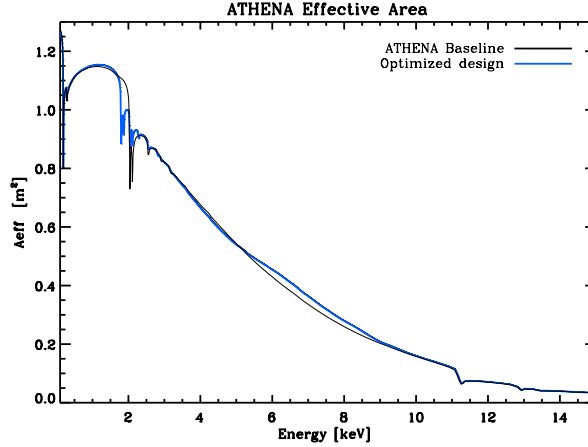


Figure 2. ATHENA optimized design and baseline. Results listed for 2 telescopes with a 10% reduction applied to account for eventual losses due to e.g. alignment and particle contaminations.

The stacked plates are bonded using direct Si-Si contact, which requires part of the surface of every substrate to be free of coating so the ribs can have direct contact to the Si wafer surface. During DC Magnetron sputtering the entire surface is coated, unless a mask is used during coating to shield part of the substrate from incoming sputtered atoms. This has previously been investigated, but the alignment of a mask for every substrate is a very cumbersome task, especially for more than 60,000 substrates.

Another solution is to use a striped resist layer, which can be removed along with any film deposited on top after coating. An example of that can be seen in figure 3, where a Ir/B₄C bilayer is deposited on a SPO substrate with a resist layer. The resist along with film is removed after coating using acetone and results in a substrate with bare Si-substrate stripes so another SPO substrate can be stacked on top.

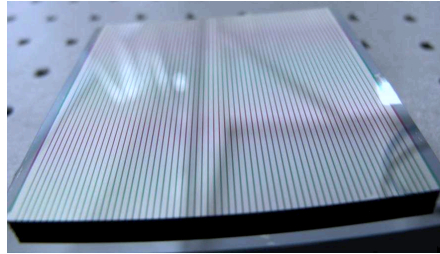


Figure 3. A coated Silicon Pore optic substrate with coating removed in a striped pattern using a resist layer.

To achieve a clean separation of coated film from the substrate in the specified striped pattern, the sputter deposited thin film needs a good adhesion to the areas of the substrate without resist layer. One factor that can be connected to bad adhesion is stress in the thin film, and the Ir/B₄C bilayer films have a compressive stress of >4 GPa during preliminary coating tests at DTU Space.

4. REDUCING STRESS IN IRIIDIUM / BORON CARBIDE BILAYERS

To reduce the stress in Ir films, we use of Cr as an underlayer between substrate and Ir. It can decrease and even remove the film stress completely. The addition of a B₄C toplayer complicates the interaction, as sputtered

B₄C films are stressed.

Investigations into the stress reducing ability of Cr on Ir/B₄C bilayers are done, with a further emphasis on the possible change in surface roughness when a Cr underlayer is introduced.

5. EXPERIMENTAL

Sample substrates were coated at DTU Space using a DC Magnetron sputtering chamber.² The substrates were mounted in the chamber between two 50 mm deep separator plates with a distance of 100 mm (see figure 4). The separator plates reduce roughness by collimating incoming sputtered atoms, so the amount of sputter atoms coming at a low angle to the substrate surface is decreased.

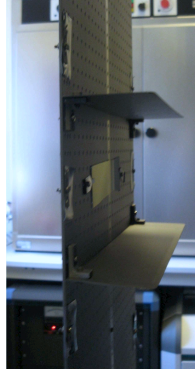


Figure 4. Side view of a mounting plate in the sputtering chamber. A Si wafer substrate is mounted in the middle between two separator plates.

Each specific film is coated on both a 20x80 mm Si wafer piece with a surface roughness of $\sigma_{\text{rms}} = 0.25$ nm for X-ray reflectometry measurements and a 5x70 mm Si wafer piece for stress measurements. All large Si wafer pieces are measured with a 8 keV Cu-K $_{\alpha}$ rotating anode at DTU Space and the data is fitted using IMD³ to determine the geometry of the coated film. The smaller Si wafer pieces were measured before and after coating using a Dektak 150 stylus measurement device, that measures the deflection of a sample and calculates the stress of a coating based on film thickness and difference in deflection before and after coating.

Two sample sets were created, each with eight different coatings as seen in table 3.

Sample	1	2	3	4	5	6	7	8	9	10	11	12	13	14	15	16
d _{Ir} [nm]	~7	~7	~7	~7	~7	~7	~7	~7	~7	~7	~7	~7	~7	~7	~7	~7
d _{B₄C} [nm]	~7	~7	~7	~7	~7	~7	~7	~7	~3.5	~3.5	~3.5	~3.5	~3.5	~3.5	~3.5	~3.5

Table 3. Overview of samples coated with Ir and B₄C.

6. DEVELOPMENT RESULTS

Figure 5 presents results from stylus point deflection measurements, with the left plot showing the change in stress with changing Cr thickness for d_{Ir} \approx d_{B₄C} \approx 7 nm. The right plot shows the change in stress with changing Cr thickness for bilayer films with d_{Ir} \approx 7 nm and d_{B₄C} \approx 3.5 nm. Each sample are represented as two dots, as both a compressive and tensile stress can be present in the film at the same time.

In both plots a clear change in stress from compressive to tensile is seen as the Cr underlayer thickness is increased.

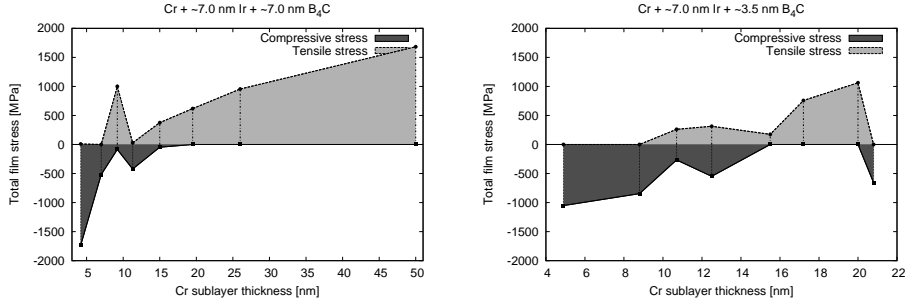


Figure 5. Plots comparing Cr thickness in a trilayer coating with the resulting total film stress. Left side compares Cr/Ir/B₄C coatings with $d_{Ir} \approx d_{B_4C} \approx 7$ nm. Right side compares Cr/Ir/B₄C coatings with $d_{Ir} \approx 7$ nm and $d_{B_4C} \approx 3.5$ nm.

The change in stress correlates with earlier investigations of Ir coatings with Cr underlayer. The stress decreases with increasing Cr thickness and the film eventually comes close to zero stress. Adding even thicker layers of Cr underneath will yield a tensile stress in the film. For Ir/B₄C bilayers of these dimensions, the film stress can be reduced to ~ 0 using a Cr underlayer with a thickness of ~ 7 nm to ~ 11 nm.

The data points for the left plot in figure 5 show a consistent curve going from compressive to tensile stress, except around the intersection point with 0 stress. Two samples show values outside the expected and outside standard error deviation. Further investigation in the low stress region is planned.

The right side plot in figure 5 shows several deviations from the expected values, but still a correlation can be seen. The intersection point with 0 stress is with Cr thickness of 12 to 14 nm. The decreased thickness of the B₄C layer has shown a considerable alteration of the structural properties of the film and thus requires a thicker Cr underlayer to minimize the total film stress.

Figure 6 shows X-ray reflectometry data from two different large Si wafer samples and the data is fitted using IMD. The left plot shows data from a trilayer of Cr/Ir/B₄C with relative thicknesses of 11 nm/7 nm/7 nm, the right plot shows data from a Cr/Ir/B₄C trilayer with relative thicknesses 4 nm/7 nm/3.5 nm.

The fit shows a surface roughness of Ir in the left plot of $\sigma_{rms} = 0.5$ nm and for Cr $\sigma_{rms} = 0.7$ nm. The surface roughness of B₄C does not affect 8 keV photons significantly in IMD simulations, so a precise value of the roughness can not be given using this measurement method. In these fits, the B₄C roughness is set to $\sigma_{rms} = 0.4$ nm. In the right plot, Ir surface roughness is significantly smaller ($\sigma_{rms} = 0.2$ nm) and so is the Cr surface roughness ($\sigma_{rms} = 0.5$ nm).

The change in Ir roughness was expected when changing the Cr thickness. Sputtered Cr films generally have a rough surface, and the roughness increases with thicker layers. That the Ir surfaces are smoother than the Cr surfaces were not expected, as the expected lower bound for film surface roughness is the surface roughness on which the film is coated. So e.g. an Ir layer coated onto a Cr surface with roughness of 0.7 nm would also give an Ir surface roughness of at least 0.7 nm. Since this is not the case in either of the two samples, the Ir and Cr combination can be suspected to give a smoothening effect on above surfaces.

For the right side plot in figure 6, the Ir surface roughness is even lower than the Si wafer substrate surface roughness (0.25 nm). This smoothening effect could be present in Cr + Ir coatings on rougher substrates, which begs for further investigation.

As the coatings done here are deposited onto normal Si wafer substrates and not wedged SPO substrates, XRR measurements of the bare substrates were done. The measurement data can be seen in figure 7 along with fits modelled using IMD.

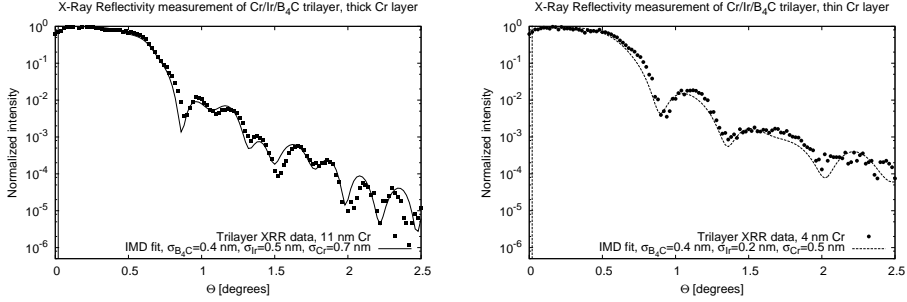


Figure 6. Plots showing X-ray reflectometry data for two different trilayer coated samples. Each data set is fitted a model from IMD to get film dimensions and surface/interface roughness values. The left side shows data from a trilayer of Cr/Ir/B₄C with relative thicknesses of 11 nm/7 nm/7 nm, the right side shows data from a Cr/Ir/B₄C trilayer with relative thicknesses 4 nm/7 nm/3.5 nm.

In the left plot is shown measurement data of a bare Si wafer substrate, and the IMD model fits to the data with a substrate surface roughness of $\sigma_{rms} = 0.25$ nm. The plot on the right shows the measurement data for a wedged SPO substrate. The IMD model fits to the data with a substrate roughness of $\sigma_{rms} = 0.45$ nm.

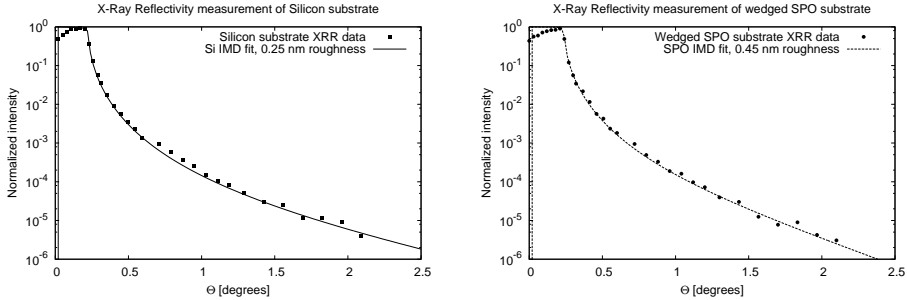


Figure 7. Plots showing X-ray reflectometry data for a bare Si wafer substrate (left side) and a wedged SPO substrate (right side). Each data set is fitted using an IMD model to get surface roughness values.

The increased roughness of wedged SPO substrates compared to bare Si wafer substrates were taken into account during the optimization procedure in section 2.1 where all surface roughness values were expected to be at least 0.45 nm.

The SiO₂ material of the wedge on the SPO substrate might yield different sputtered film properties due to different interatomic spacing in the amorphous surface. All possible coating candidates will be tested on proper wedged substrates in the next months.

7. CONCLUSION

A preliminary coating design optimization of the ATHENA optic has been shown, using an analytical approach to achieve optimum coating recipes for the outer five mirror module rows. The optimized coating uses linearly graded multilayers to increase the effective area around 6 keV by ~ 5 %.

Additionally, trilayer coatings of Cr/Ir/B₄C were deposited onto Si wafer substrates to investigate film stress and surface roughness properties. A correlation between Cr thickness and film stress has been found, where a Cr

underlayer can remove most of the stress in a Ir/B₄C film. A thicker Cr underlayer to reduce stress is necessary when decreasing the B₄C layer thickness in a Ir/B₄C bilayer. Finally, XRR measurements have shown that although Cr surface is relatively high, the surface roughness of Ir layers deposited on top of Cr were consistently lower.

8. FUTURE INVESTIGATIONS

Results on coating design for ATHENA presented here are preliminary. Several aspects of the coating design optimization are undergoing further investigation and improvement. Other material combinations will be investigated as well as the possibility of changing the amount of mirror modules coated with trilayer vs. multilayers.

Work to be done in coating development includes the introduction of reactive sputtering using N₂ gas^{4,5} to reduce film stress and surface/interface roughness as well as using honeycomb collimation⁶ during sputtering. Film stress in multilayers and the removal of stress using Cr underlayers will also be investigated. X-ray reflectometry and X-ray scattering will be performed at BESSY. Additional measurement techniques will be used, such as cross-sectional TEM, Atomic Force Microscopy and X-ray fluorescence.

REFERENCES

- [1] Wallace, K., Bavdaz, M., and Gondoin, P., "Silicon pore optics development," *Proceedings of SPIE* **7437**.
- [2] Jensen, C., Christensen, F., Chen, H., Smitt, E., and et al, "Multilayer coating facility for the HEFT hard x-ray telescope," *Proceedings of SPIE* **4496**, 104–108 (Jan. 2002).
- [3] Windt, D., "IMD—Software for modeling the optical properties of multilayer films," *Computers in Physics* **12**, 360–370 (Jan. 1998).
- [4] Windt, D., "Reduction of stress and roughness by reactive sputtering in W/B₄C X-ray multilayer films," *Proceedings of SPIE* **6688** (Jan. 2007).
- [5] Bellotti, J. and Windt, D., "Depth-graded Co/C multilayers prepared by reactive sputtering," *Proceedings of SPIE* **7437** (Jan. 2009).
- [6] Anette, V. and Carsten, P., "Collimated Magnetron Sputter Deposition for Mirror Coatings," *X-Ray Optics and Instrumentation* **2008** (Jan. 2008).

APPENDIX B

X-ray optics for axion helioscopes

Publication printed in *Proc. SPIE, Optics for EUV, X-Ray, and Gamma-Ray Astronomy VI*.

X-ray optics for axion helioscopes

Anders C. Jakobsen^a, Michael J. Pivovarov^b and Finn E. Christensen^a

^aDanish Technical University (DTU) Space, Elektrovej 327, DK-2800 Kgs. Lyngby, Denmark

^bLawrence Livermore National Laboratory, 7000 East Avenue, Livermore, CA 94550, USA

ABSTRACT

A method of optimizing grazing incidence x-ray coatings in ground based axion helioscopes is presented. Software has been developed to find the optimum coating when taking both axion spectrum and Micromegas detector quantum efficiency into account. A comparison of the relative effective area in the telescope using different multilayer material combinations is produced. Similar methods are used for IAXO, a planned axion helioscope. Additionally, the optimal focal length is modelled while taking into account the least possible background contribution from the detector.

Keywords: X-ray optics, axion, multilayer coatings

1. INTRODUCTION

Axions are theoretical particles created by the Primakoff effect¹ from photons interacting with strong electric and magnetic fields. An obvious place to look for axions would then be our own sun. The particles are weakly interacting, so detection becomes a challenge. A solution is to use the Primakoff effect again to reconvert the axion into a photon using a strong magnetic field and subsequently detecting the photon in an x-ray detector as seen in figure 1.

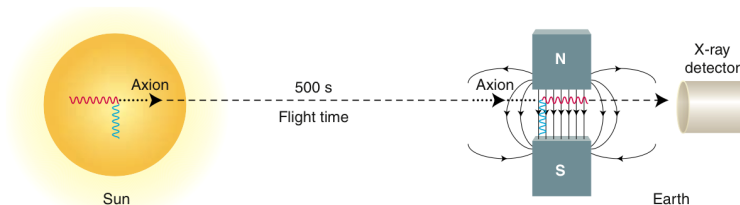


Figure 1. Diagram of axions created by the Primakoff effect in the sun, travelling to Earth and getting detected using a strong magnetic field and a detector.

In the past 30 years the hunt for axions as a solution to CP violation in particle physics and a possible candidate for dark matter, have required larger and more sensitive instruments. The third and latest generation of helioscopes for axion detection is the CERN Axion Solar Telescope (CAST),²⁻⁵ consisting of a LHC prototype magnet and low background MicroMegs detectors.⁶

The main problem is to distinguish a small signal amidst the background, which largely comes from the detector. The magnetic bores on CAST are 50 mm wide, so a detector to cover a bore consequently becomes large. The detector area is proportional to the background squared. A solution is to reflect the x-ray photons coming from the bore in an x-ray optic and onto a much smaller detector. In the next section, the design of such an optic is explained.

Further author information:

A.C.J.: E-mail: jakobsen@space.dtu.dk, Telephone: +45 4525 9735

2. CAST TELESCOPE GEOMETRY

The x-ray optic for CAST is of a relatively small size, as only photons coming out of a 50 mm bore will be reflected and the focal length is limited to 1.5 m due to one of the side walls in the CAST building.

An already proven technology for building Wolter I type optics for space based applications is used in the NuSTAR telescope.^{7,8} Slumped glass pieces, each 0.2 mm thick are placed on a SiC mandrel and graphite spacers are used to hold each piece in place at the correct angle. Two stacks of slumped glass substrates with graphite spacers are required for the double reflection geometry of the Wolter I optic. The optic for CAST will be made from spare NuSTAR glass, but only using 1/6th of the full circle and with an adjusted mandrel.

The angle of each glass substrate depends on the focal length, l , and radius, r , and is described as $\tan 4\alpha = r/l$. Every layer put on the mandrel has to have a width wide enough to cover the bore opening which sets a lower limit on the radius of the innermost glass layer. Each subsequent glass substrate is mounted on top of the earlier so there is no overlap. The resulting diagram for an optic optimized for a 50 mm bore opening and 1.5 m focal length is shown in figure 2.

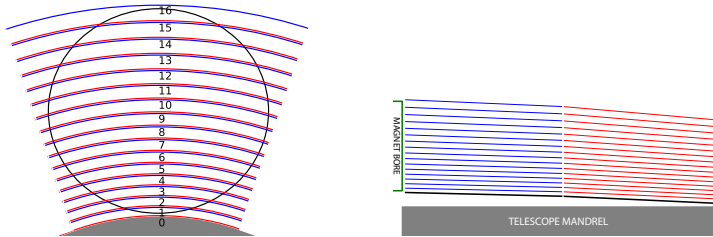


Figure 2. Diagrams of glass layering in Wolter I optic for the CAST axion helioscope. **Left:** Optic as seen from front. The circle shows the magnet bore opening compared to the optic. **Right:** Optic seen from side. Horizontal axis is compressed to show the tilt of each glass layer.

3. CAST COATINGS

Optimal coatings were calculated by taking into consideration detector efficiency, axion spectrum at each optical glass angle in the telescope. Axion spectrum is given by theory as a curve reminiscent of black body radiation between 0.1 and 10 keV as seen in figure 3.

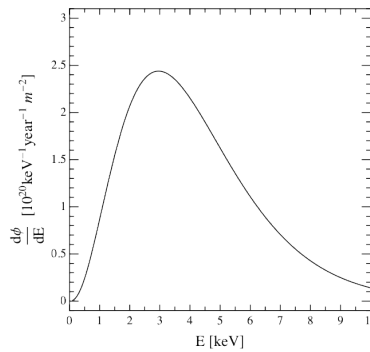


Figure 3. Solar axion flux spectrum at Earth, originating from the Primakoff process.

Material types investigated were multilayers of W/B₄C, W/Si, Pt/B₄C, Ni/B₄C as well as single layers of W, Pt, Ir and Ni. W/B₄C and W/Si are well understood coatings for x-ray reflectivity and considerably less expensive to use W than Pt or Ir. Using B₄C instead of Si as the light material will give increase reflectivity at 1 - 4 keV, but also gives slightly higher stress in the coating.⁹ Ni/B₄C coatings are not well understood and can give a high interfacial roughness between light and heavy material, but performs similar to W/B₄C and Ir/B₄C at 1-10 keV.

At a given glass substrate angle, α , the coating geometry was optimized by trying every combination in a parameter space of n (number of bilayers), d_{\min} (minimum bilayer thickness), d_{\max} (maximum bilayer thickness) and Γ (ratio between heavy and light material in a bilayer.) For every combination, the x-ray reflectivity was calculated using IMD¹⁰, multiplied with axion spectrum and detector efficiency and integrated to give a figure of merit (eqn. 1). The F.O.M. found in the parameter space is chosen as the optimal coating recipe for the given angle and focal length.

$$F.O.M. = \int_{0.1}^{10} R^2(\alpha, E) Q E_{det}(E) S_{axion} dE \quad (1)$$

Output for optimized coating recipes for a w/B₄C material combination can be seen on the left side of figure 4. Each glass substrate layer should have between 2 and 6 bilayers with d-spacings between 50 and 260 Å.

A comparison of material combinations is seen on the right side of figure 4. The effective areas are calculated using eqn 2. Multilayers are seen to easily outperform the single layer coatings. Best performing are W/B₄C and Ni/B₄C multilayers.

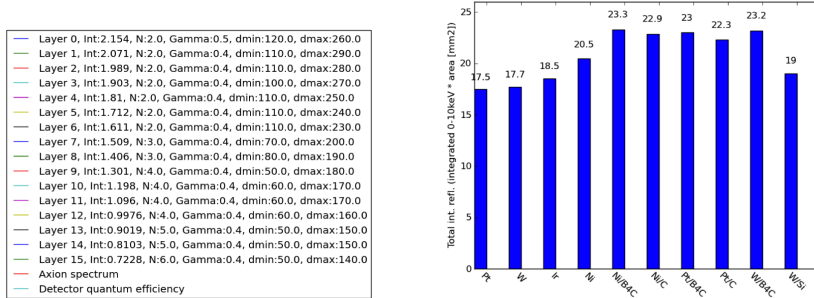


Figure 4. Results of multilayer coating optimization for the CAST Wolter I optic. **Left:** Optimized recipe for each layer in the optic. **Right:** Effective area comparison between each optimized material combination recipe.

$$A_{effective} = \sum_{i=1}^N \int_{0.1}^{10} R_i^2(\alpha, E) Q E_{det}(E) S_{axion} A_i dE \quad (2)$$

4. TELESCOPES FOR THE IAXO HELIOSCOPE

A next generation axion helioscope currently in the proposal stage is the International AXion Observatory, IAXO.^{11–13} It is a direct successor to CAST, with much larger magnet bores, bigger super conducting magnet and possibility of higher inclination, meaning it can measure axions coming from the sun 12 hours a day. An illustration can be seen in figure 5

Optimal coatings were calculated by taking into consideration detector efficiency, axion spectrum at each optical glass angle in the telescope. The telescope geometry, glass substrate angles and positions were first computed for focal lengths 4, 5, 6, 7, 8, 9 and 10 m. For each focal length, the x-ray reflectivity at 1-10 keV

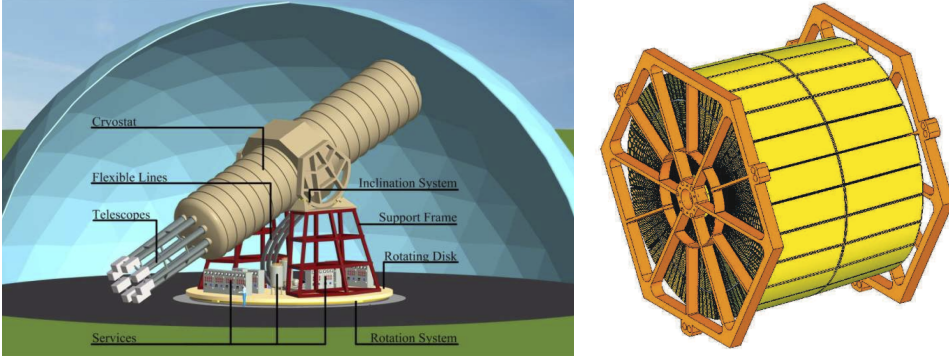


Figure 5. IAXO, a next generation axion helioscope. **Left:** Model of proposed IAXO setup. Superconducting magnet (cryostat) with 8 bores each 600 mm in diameter placed on a rotating platform to track the sun. **Right:** Model of a single Wolter I type optic for IAXO. One optic will be placed on the end of each bore.

for each coating material combination and thin film geometry were compared. Axion spectrum and detector efficiency were included in the comparison.

For a focal length of 4 m and bore diameter of 0.6 m, 110 glass substrate layers are needed to focus incoming x-rays to the same spot. At increasing focal length, even more glass layers and for 10 m focal length, required glass layers reach 235. To simplify the optimization and eventual coating deposition, the number of coating 'recipes' are fixed at 10, so only 10 different coatings will be required for a telescope.

5. IAXO TELESCOPE FOCAL LENGTH

To calculate the total telescope efficiency at a given focal length, the following equation was used.

$$\text{Throughput}_i = \frac{R_i^2 * A_{cs} * 0.8}{A_{bore}} \quad (3)$$

The fraction of photons reflected by layer i could be found using the cross sectional area of a layer opening and the total area of the bore opening. The factor 0.8 was used to include obscurations in the form of substrate spacers.

To find the optimal focal length, a non traditional approach was used. For a generic x-ray optic, the longer focal length gives a higher effective area, which was also the case here. But at increasing focal lengths, the focused spot also becomes bigger as a result of optic HPD (Half Power Diameter). Since the goal was to find a signal in the background, it was desirable to use a detector as small as possible, considering that the area of the detector is proportional to the background. In order to minimize detector area, it was therefore required to minimize the focused spot size, while also maximizing the effective area of the telescope. Spot area was determined using the enclosed energy diameter (EED) of the telescope at focal length f using a telescope HPD of 2 arc seconds for the worst case scenario and 1 arc second for the best case. EED of the sun (EED_{sun}) was also included using an HPD of 3.61 arc minutes. A combined EED of $(EED^2 + EED_{\text{sun}}^2)^{\frac{1}{2}}$ was used to calculate the area of the spot.

A new figure of merit, which also includes the square root of the spot arean was used for optic optimization:

$$F.O.M. = \frac{\int_{0.1}^{10} R^2(\alpha, E) Q E_{det}(E) S_{axion} dE}{\sqrt{a}} \quad (4)$$

The parameter space used for optimization was identical to that used for the CAST optic, but with a variety of focal lengths from 4 m to 10 m and with only one material combination (W/B₄C). The result can be seen in figure 6. A notable difference in F.O.M. can be seen as focal length increases, resulting in larger focused spot. The optimal focal length is seen to be 5 m.

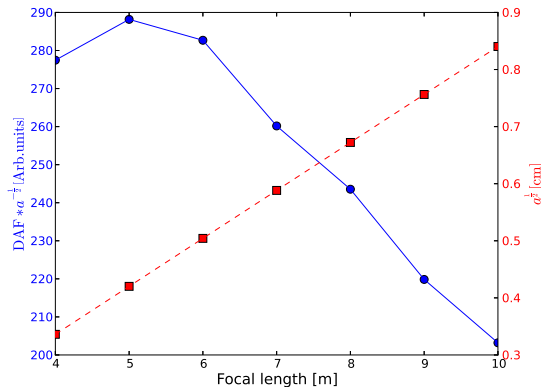


Figure 6. Result of focal length optimization. Circles show the throughput divided by the square root of the focused spot area. Squares show the square root of the focused spot area.

6. CONCLUSION

Software was developed to optimize geometry and multilayer coatings for the CAST axion helioscope. By including both detector quantum efficiency and axion spectrum in the optimization procedure, a true value of coating efficiency can be found. Maximum throughput can be achieved using either Ni/B₄C or W/B₄C multilayer coatings with 2-6 bilayers and d-spacings of 5-26 nm.

An extension of same software was used to find the optimal focal length of optics for the next generation IAXO axion helioscope. Using W/B₄C multilayer coatings and including the size of the focused spot in the calculations, an optimal focal length of 5 m was found.

REFERENCES

- [1] Primakoff, H., “Photo-Production of Neutral Mesons in Nuclear Electric Fields and the Mean Life of the Neutral Meson,” *Physical Review* **81**, 899–899 (Mar. 1951).
- [2] Iguaz, F. J., “The CAST experiment: status and perspectives,” *arXiv.org* (Oct. 2011).
- [3] Ferrer-Ribas, E., Arik, M., Aune, S., Barth, K., Belov, A., Borghi, S., Bräuninger, H., Cantatore, G., Carmona, J. M., Cetin, S. A., Collar, J. I., Dafni, T., Davenport, M., Eleftheriadis, C., Elias, N., Ezer, C., Fanourakis, G., Friedrich, P., Galan, J., Garcia, J. A., Gardikiotis, A., Gazis, E. N., Gerasis, T., Giomataris, I., Gninenko, S., Gomez, H., Gruber, E., Guthörl, T., Hartmann, R., Haug, F., Hasinoff, M. D., Hoffmann, D. H. H., Iguaz, F. J., Irastorza, I. G., Jacoby, J., Jakov vcić, K., Karuza, M., Königsmann, K., Kotthaus, R., Kremar, M., Kuster, M., Lakic, B., Laurent, J. M., Liolios, A., Ljubičić, A., Lozza, V., Lutz, G., Luzon, G., Morales, J., Niinikoski, T., Nordt, A., Papaevangelou, T., Pivovarov, M. J., Raffelt, G., Rashba, T., Riege, H., Rodriguez, A., Rosu, M., Ruz, J., Savvidis, I., Silva, P. S., Solanki, S. K., Stewart, L., Tomas, A., Tsagri, M., van Bibber, K., Vafeiadis, T., Villar, J., Vogel, J. K., Yildiz, S. C., and Zioutas, K., “Results and perspectives of the solar axion search with the CAST experiment,” *arXiv.org* (Sept. 2012).

- [4] Papaevangelou, T., “Status report of the CAST Experiment & Running in 2013-2014,” Tech. Rep. CERN-SPSC-2012-028. SPSC-SR-106, Geneva (Oct. 2012).
- [5] Barth, K., Belov, A., Beltran, B., Bräuninger, H., Carmona, J. M., Collar, J. I., Dafni, T., Davenport, M., Di Lella, L., Eleftheriadis, C., Englhauser, J., Fanourakis, G., Ribas, E. F., Fischer, H., Franz, J., Friedrich, P., Galan, J., Garcia, J. A., Gerasis, T., Giomataris, I., Gninenko, S., Gomez, H., Hassinoff, M. D., Heinsius, F. H., Hoffmann, D. H. H., Irastorza, I. G., Jacoby, J., Jakovcic, K., Kang, D., Königsmann, K., Kotthaus, R., Kousouris, K., Krcmar, M., Kuster, M., Lakic, B., Liolios, A., Ljubičić, A., Lutz, G., Luzon, G., Miller, D. W., Papaevangelou, T., Pivovarov, M. J., Raffelt, G., Redondo, J., Riege, H., Rodriguez, A., Ruz, J., Savvidis, I., Semertzidis, Y., Stewart, L., van Bibber, K., Vieira, J. D., Villar, J. A., Vogel, J. K., Walckiers, L., and Zioutas, K., “CAST constraints on the axion-electron coupling,” *arXiv.org* (Feb. 2013).
- [6] Tomas, A., Ferrer-Ribas, E., Luzon, G., Gomez, H., Ruz, J., Dafni, T., Segui, L., Fanourakis, G., Yildiz, S. C., Galan, J., Giomataris, I., Aune, S., Gerasis, T., Gardikiotis, A., Morales, J., Iguaz, F. J., Garcia, J. A., Rodriguez, A., Papaevangelou, T., Irastorza, I. G., and Vafeiadis, T., “The new micromegas X-ray detectors in CAST,” *X-Ray Spectrom.* **40**(4), 240–246 (2011).
- [7] Harrison, F. A., Craig, W. W., Christensen, F. E., Hailey, C. J., Zhang, W. W., Boggs, S. E., Stern, D., Cook, W. R., Forster, K., Giommi, P., Grefenstette, B. W., Kim, Y., Kitaguchi, T., Koglin, J. E., Madsen, K. K., Mao, P. H., Miyasaka, H., Mori, K., Perri, M., Pivovarov, M. J., Puccetti, S., Rana, V. R., Westergaard, N. J., Willis, J., Zoglauer, A., An, H., Bachetti, M., Barrière, N. M., Bellm, E. C., Bhalariao, V., Brejnholt, N. F., Fuerst, A., Dufour, F., Liebe, C. C., Markwardt, C. B., Nynka, M., Vogel, J., Walton, D. J., Wik, D. R., Alexander, D. M., Cominsky, L. R., Hornschemeier, A. E., Hornstrup, A., Kaspi, V. M., Madejski, G. M., Matt, G., Molendi, S., Smith, D. M., Tomsick, J. A., Ajello, M., Ballantyne, D. R., Baloković, M., Barret, D., Bauer, F. E., Blandford, R. D., Brandt, W. N., Brenneman, L. W., Chiang, J., Chakraborty, D., Chenevez, J., Comastri, A., Dufour, F., Elvis, M., Fabian, A. C., Farrah, D., Fryer, C. L., Gotthelf, E. V., Grindlay, J. E., Helfand, D. J., Krivonos, R., Meier, D. L., Miller, J. M., Natalucci, L., Ogle, P., Ofek, E. O., Ptak, A., Reynolds, S. P., Rigby, J. R., Tagliaferri, G., Thorsett, S. E., Treister, E., and Urry, C. M., “THE NUCLEAR SPECTROSCOPIC TELESCOPE ARRAY (NuSTAR) HIGH-ENERGY X-RAY MISSION,” *The Astrophysical Journal* **770**, 103 (May 2013).
- [8] Christensen, F. E., Jakobsen, A. C., Brejnholt, N. F., Madsen, K. K., Hornstrup, A., Westergaard, N. J., Momberg, J., Koglin, J., Fabricant, A. M., Stern, M., Craig, W. W., Pivovarov, M. J., and Windt, D., “Coatings for the NuSTAR mission,” in [*SPIE Optical Engineering + Applications*], O’Dell, S. L. and Pareschi, G., eds., 81470U–81470U–19, SPIE (Sept. 2011).
- [9] Jakobsen, A. C., Ferreira, D. D. M., Christensen, F. E., Shortt, B., Collon, M., and Ackermann, M. D., “Preliminary coating design and coating developments for ATHENA,” in [*Optics for EUV, X-Ray, and Gamma-Ray Astronomy V*], 81470T–8, SPIE (Sept. 2011).
- [10] Windt, D. L., “IMD—Software for modeling the optical properties of multilayer films,” *Computers in Physics* **12**, 360 (1998).
- [11] Irastorza, I. G., Avignone, F. T., Caspi, S., Carmona, J. M., Dafni, T., Davenport, M., Dudarev, A., Fanourakis, G., Ferrer-Ribas, E., Galan, J., Garcia, J. A., Gerasis, T., Giomataris, I., Gomez, H., Hoffmann, D. H. H., Iguaz, F. J., Jakovcic, K., Krcmar, M., Lakic, B., Luzon, G., Pivovarov, M., Papaevangelou, T., Raffelt, G., Redondo, J., Rodriguez, A., Russenschuck, S., Ruz, J., Shilon, I., Ten Kate, H., Tomas, A., Troitsky, S., van Bibber, K., Villar, J. A., Vogel, J., Walckiers, L., and Zioutas, K., “Towards a new generation axion helioscope,” *arXiv.org* (Mar. 2011).
- [12] Irastorza, I. G., Avignone, F. T., Cantatore, G., Caspi, S., Carmona, J. M., Dafni, T., Davenport, M., Dudarev, A., Fanourakis, G., Ferrer-Ribas, E., Galan, J., Garcia, J. A., Gerasis, T., Giomataris, I., Gninenko, S., Gomez, H., Hoffmann, D. H. H., Iguaz, F. J., Jakovcic, K., Krcmar, M., Lakic, B., Luzon, G., Lindner, A., Pivovarov, M., Papaevangelou, T., Raffelt, G., Redondo, J., Russenschuck, S., Ruz, J., Shilon, I., Ten Kate, H., Tomas, A., Troitsky, S., van Bibber, K., Villar, J. A., Vogel, J., Walckiers, L., and Zioutas, K., “The International Axion Observatory (IAXO),” *arXiv.org* (Jan. 2012).
- [13] Vogel, J. K., Avignone, F. T., Cantatore, G., Carmona, J. M., Caspi, S., Cetin, S. A., Christensen, F. E., Dael, A., Dafni, T., Davenport, M., Derbin, A. V., Desch, K., Diago, A., Dudarev, A., Eleftheriadis, C., Fanourakis, G., Ferrer-Ribas, E., Galan, J., Garcia, J. A., Garza, J. G., Gerasis, T., Gimeno, B., Giomataris, I., Gninenko, S., Gomez, H., Hailey, C. J., Hiramatsu, T., Hoffmann, D. H. H., Iguaz, F. J., Irastorza, I. G.,

Isern, J., Jaeckel, J., Jakovcic, K., Kaminski, J., Kawasaki, M., Krcmar, M., Krieger, C., Lakic, B., Lindner, A., Liolios, A., Luzon, G., Ortega, I., Papaevangelou, T., Pivovarov, M. J., Raffelt, G., Redondo, J., Ringwald, A., Russenschuck, S., Ruz, J., Saikawa, K., Savvidis, I., Sekiguchi, T., Shilon, I., Silva, H., ten Kate, H. H. J., Tomas, A., Troitsky, S., van Bibber, K., Vdrine, P., Villar, J. A., Walckiers, L., Wester, W., Yildiz, S. C., and Zioutas, K., “IAXO - The International Axion Observatory,” *arXiv.org* (Feb. 2013).

